Journal of Power Sources 465 (2020) 228262

Contents lists available at ScienceDirect

Journal of Power Sources

journal homepage: www.elsevier.com/locate/jpowsour

Aluminum phosphide as a high-performance lithium-ion battery anode

Hsuan-Peng Lin, Kuan-Ting Chen, Che-Bin Chang, Hsing-Yu Tuan *

Department of Chemical Engineering, National Tsing Hua University, Hsinchu, 30013, Taiwan

HIGHLIGHTS

- Aluminum phosphide (AlP) as an anode material for lithium-ion batteries for the first time.
- AlP electrode has a reversible specific capacity of 1463 mA h g^{-1}.
- AlP electrode has a 650 mA h g^{-1} over 2000 cycles at 1C.
- Both coin-type and pouch-type full cells with AlP anodes are assembled.

GRAPHICAL ABSTRACT

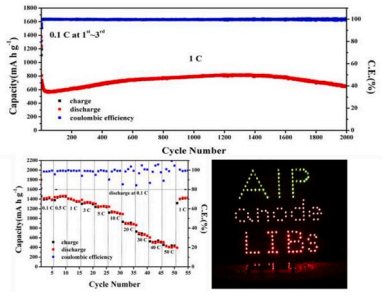

ARTICLE INFO

Keywords:
Aluminum
Phosphide
Lithium ion batteries
Conversion
Ball milled
Storage

ABSTRACT

We report aluminum phosphide (AlP) as an anode material for lithium-ion batteries for the first time. AlP was prepared from aluminum and black phosphorus *via* a ball milling method, and further milled with carbon nanotubes to enhance its conductivity. The AlP electrode possesses excellent electrochemical properties, having a reversible specific capacity of 1463 mA h g^{-1} at 0.1C (1C = 1850 mA h/g), 650 mA h g^{-1} without obviously decay over 2000 cycles at 1C, and high-rate capabilities up to 50C. Both coin-type and pouch-type full cells with AlP anodes are assembled and demonstrate as a reliable power supply to drive electronic devices. This study shows that AlP is an anode material with characteristics including high capacity, ultra-long cycling stabiltiy and high rate capabilities, making it a new class of graphite alternative for LIB anodes.

1. Introduction

Lithium-ion batteries (LIBs) are extensively applied as renewable power source for portable electronic devices and electric vehicles (EV) [1–5]. However, traditional LIB configuration, i.e. graphite as anodes coupled with lithium metal oxide as cathodes, can't achieve the requisites for higher battery energy density [6,7]. The use of high theoretical Li capacity materials over 1000 mA h g^{-1} to replace low capacity of graphite is (372 mA h g^{-1}) is regarded as a configuration for the next generation of LIBs [8–11]. Recently, phosphorus (P) is considered as a promising graphite alternative not only for its extremely high specific capacity with Li (2596 mA h g^{-1}) and for their earth abundance. However, the drastic volume expansion/shrinking (>300%) during a lithiation/delithiation process causes the decrease of anode capacities. In addition, its extremely low electrical conductivity and relatively unknown synthetic chemistry remain unsolved issues [12–23].

As a phosphorus-based anode material for LIB, metal phosphides have less volume change compared to phosphorus while reacting with Li ions and still have a higher capacity relative to graphite anode. In addition, metal phosphides have safe working potentials, low

* Corresponding author.
E-mail address: hytuan@che.nthu.edu.tw (H.-Y. Tuan).

https://doi.org/10.1016/j.jpowsour.2020.228262
Received 25 February 2020; Received in revised form 15 April 2020; Accepted 25 April 2020
Available online 11 May 2020

polarization, and excellent thermal stability. The mechanism of MPx is generally considered as the follows.

$$MP_x + 3xLi \rightarrow M^0 + xLi_3P$$

According to this equation, each P atom can react with three Li ions to form Li_3P along with bond cleavage between metal and phosphorus. Nanoscale Li_3P and Li_xM are usually formed as the lithium-alloys, which can contribute to electrode capacity. Metal phosphides such Mn–P, V–P, Sn–P, Ni–P, Cu–P, Fe–P, Co–P, Zn–P, Ge–P, Mo–P, Se_4P4, GaP, and so on, are reported as lithium ion battery anodes [24–32]. In general, in order to achieve higher capacities, phosphorus-rich metal phosphide are preferred. However, the use of high-capacity phosphide may increase the reaction complexity since both elements can react with Li, resulting in relatively poor cycling stability. For example, NiP_3 can deliver an initial reversible capacity of 1475 mA h g^{-1}, but the cycling stability is poor [33]. Therefore, these electrodes need to form carbon composites via high-temperature annealing or ball milling to improve their cycling performance [34,35].

The selection of metal counterpart of metal phosphide is crucial to attain stable conversion reactions phosphide compound. Aluminum (Al) is an attractive metal counterpart for LIB phosphorus anodes due to the following reasons. First, Al has relatively smaller volume change (~97%) compared with other high-capacity elemental materials during lithium insertion/extraction. Second, Al has low potential plateau (~0.19–0.45 V vs. Li/Li^+) that can maintain the operating voltage. Third, Al has high electric conductivity (3.78×10^7 S m^{-1}) and high diffusivity of Li-ions (6×10^{-12} cm^2 s^{-1}). Finally, as an anode materials for LIBs, Al has fine specific theoretical capacity (993 mA h g^{-1} for LiAl, 1490 mA h g^{-1} for Li_3Al_2, and 2235 mA h g^{-1} for Li_9Al_4) [36–42].

Herein, we report aluminum phosphide (AlP) as a new high-capacity lithium ion battery anode that shows a high capacity (>1000 mAh/g) with a high cycling life (2000 cycles). Nanosized AlP powder is fabricated by mixing Al with P via a facile mechanical ball milling method (MBMM). The AlP electrodes show characteristics of high capacity, ultralong cycle life, and high rate capabilities. The electrodes have high reversible capacity of 1463 mA h g^{-1} at the 2nd cycle and maintained 1179 after 260 cycles at a charge current density of 0.185 A g^{-1} (1C = 1850 mA h g^{-1}). Importantly, it has a capacity of 650 mA h g^{-1} after 2000 cycles at 1.85 A g^{-1} (1C) and a high rate capacity of 450 mA h g^{-1} at 92.5 A g^{-1} (50C). The full cells were also assembled by using AlP as an anode coupled with $LiFePO_4$ as a cathode to evaluate its practical performance.

2. Experimental sections

2.1. Materials

All chemicals and solvents were used as received. Aluminum nanopowder (Al, 99.9%, metal basis) was purchased from US Research Nanomaterials, red phosphorus powder (P, 98.9%, amorphous, metal basis) was purchased from Alfa Aesar, multi-walled carbon nanotube (MWCNT, 90%) was purchased from TCNT, poly (acrylic acid) (PAA, average M_v~3000000) was purchased from Aldrich, methanol (CH_3OH, low water) was purchased from J.T. Baker. Lithium hexafluorophosphate ($LiPF_6$), fluoroethylene carbonate (FEC, $C_3H_3FO_3$), diethyl carbonate (DEC, $C_5H_{10}O_3$), ethylene carbonate (EC, $C_3H_4O_3$), dimethyl carbonate (DMC, $C_3H_6O_3$), lithium metal foil, copper metal foil (0.01 mm), membrane, super-P, Ketjen black, and coin-type cell CR2032 were purchased from Shining Energy Co. Ltd. Commercial $LiFePO_4$ cathode materials were purchased from Vista Advance Technology. The components of the pouch type battery were purchased from MTI Shenzhen Kejingstar Technology. LED bulbs and fan were purchased from an electronic equipment and appliance store.

2.2. Characterization

The structural investigation of the as-synthesized products were examined by using X-ray diffraction (XRD, Rigaku Ultima IV X-ray diffractometer, Cu Kα λ = 1.54178 Å, scanning rate 1°/min), Confocal Micro-Raman Spectroscopy (Raman, Horiba Jobin Yvon, LABRAM HR 800 UV) with a radiation of 514 nm, field emission scanning electron microscope (SEM, Hitachi SU8010), transmission electron microscope (TEM, Philips TECHAI20), and high resolution transmission electron microscope (HRTEM, JEOL JEM-3000F and JEOL JEM-ARM200FTH). The chemical bonds of metals were analyzed by using X-ray photoelectron spectroscopy (XPS, ULVAC-PHI PHI 5000 Versaprobe II). The electrochemistry impedance spectroscopy test and the cyclic voltammetry test were measured by using VMP3 (Bio-Logic Science Instruments).

2.3. Synthesis of AlP composites

Firstly, the black phosphorus was transferred from the red phosphorus *via* high energy mechanical ball milling method (HEMM) at 600 rpm for 6 h under argon. Secondly, AlP was synthesized with the aluminum powder and the black phosphorus *via* HEMM at 600 rpm for 6 h under argon. The Al powder and the black P was mixed with a mole ratio of 1:1 (64.8 mg–74.4 mg). Finally, AlP/CNT mixture was fabricated with AlP powder and MWCNT *via* HEMM at 200 rpm for 24 h under argon. AlP and MWCNT were mixed with a mass ratio of 2:1. AlP/CNT mixture was stored in an argon-filled glovebox to keep it from water and oxygen.

2.4. Battery assembly and electrochemical characterization

The electrode was prepared by mixing AlP as an active material (53.3 wt%), MWCNT (26.7 wt%) as a conductive material and PAA as binder (20 wt%) for 24 h in anhydrous methanol solvent to form a homogeneous slurry. All of those steps were conducted in an argon-filled glovebox. The slurry was then cast on a Cu foil. The electrode was dried at 50 °C for 5 min under Air and 150 °C for 1 h under argon to remove residual water and then pressed by a rolling machine afterward. For calculating the specific capacity, materials were measured the accurate weight of electrode by using a microbalance (Sartorius SE2) with 0.1 μg resolution. Typical total mass loading on Cu foil is ~1 mg/cm^2. The coin-type half cells (CR2032) contained the electrode, Li metal foil, microporous polyethylene separator soaked in electrolyte, and case were prepared in an argon-filled glovebox. The electrolyte solution was 1 M $LiPF_6$ in fluoroethylene carbonate/diethyl carbonate (1:1 vol%). The electrochemical performance of half cells was measured by the galvanostatic cycling of the coin-type half cells (CR2032) with AlP as the working electrode and the lithium metal foil as the counter electrode. The electrochemical performance data of AlP was collected using a Maccor Series 4000 battery test system within 0.1C–50C at the voltage of 0.01–3.2 V (vs. Li/Li^+).

The coin-type full cell was assembled by using AlP as an anode and $LiFePO_4$ as a cathode with an A/C ratio of ~1.1, the capacities of the anode and the cathode were ~1.7 mA h and ~1.55 mA h, respectively. For a pouch-type full cell assembly, firstly, AlP anode and $LiFePO_4$ cathode electrodes were cut into the area of 18 cm^2 (6 cm × 3 cm). Next, nickel tab and aluminum tab were connected to the anode and the cathode, respectively. Then, the anode, the cathode, and the separator were piled together and put into an aluminum bag, followed by the injection of electrolyte and the vacuum sealing. The electrochemical performance of AlP–$LiFePO_4$ full cells was measured by using a Maccor Series 4000 battery test system under 0.1C within the voltage between 1 and 4 V. All the current calculation was based on the weight of an active material.

3. Results and discussions

Fig. 1a shows the schematically crystallographic phase change before and after the HEMM. After the ball milling, the aluminum phosphide (sphalerite structure) had a different type crystallographic phase from black phosphorus (orthorhombic) and aluminum (face-centered cubic). As shown in Fig. 1b, the color of AlP powder was dark brown, quite different from black color of phosphorus powder and gray color of aluminum powder. In order to confirm the phase purity of AlP, Fig. 1c presents the XRD pattern which is the crystalline sphalerite structure of AlP (space group: $F\bar{4}3m$, a = 5.421 Å; JCPDS #800013). The XRD pattern was dominated by five main diffraction peaks at 28.5°, 47.4°, 56.2°, 69.3°, and 76.5°. No other phase and impurities were observed. As shown in Fig. 1d, the crystallinity of AlP increased as prolonging the ball milling time from 30 min to 6 h. The 6-h milled product was selected as the active material for electrochemical testing.

Fig. 2a and b shows the SEM and HRTEM image of AlP, respectively. AlP clustered together with no specific morphology after the ball milling. The corresponding SAED pattern is shown in Fig. 2c. There were three main diffraction rings in the SAED pattern. Those diffraction rings were indexed respectively to (111), (220), and (311) lattice planes of sphalerite crystal structure of AlP, which matched to the same crystal structure observed in the XRD measurement.

In order to enhance the performance of the active material, MWCNT was introduced as a conductive agent and mixed with AlP *via* HEMM as shown in Fig. 2d. It can be seen that MWCNT was disintegrated into conductive carbon and form uniform carbon composites with AlP. Fig. 3a and b shows the X-ray photoelectron spectroscopy (XPS) spectrum peak at 74.2 eV, which was the Al–P bond on Al-2p orbit. The XPS peaks at 129.5 eV and 132.2 eV on P-2p orbit were also not affected (Fig. S3) [43–49]. The XPS clearly indicated that the HEMM only mix AlP and MWCNT without chemical reaction. Fig. 3c–f shows the SEM image of AlP/CNT mixture and corresponding energy dispersive spectroscopy (EDS) elemental mappings of aluminum, phosphorus, and carbon (with the white color, red color, and green color), respectively.

The electrochemical performance of AlP was tested in a CR2032 coin cell. The counter electrode was lithium metal foil and the operating voltage range was within 0.01–3.2 V vs. Li^+/Li. A galvanostatic cycling test of AlP with a current density of 0.185 A g^{-1} (0.1C) was shown in Fig. 4a. The first cycle exhibited that discharge and charge specific capacities were 1668 and 1496 mA h g^{-1}, respectively, with a high first cycle coulombic efficiency (C.E.) of 87.7%. The irreversible capacity was mostly caused by three reasons: the side reactions happened during the reaction, some Li^+ were trapped in the defective structure, and the solid electrolyte interface (SEI) layer was formed during the lithiation/delithiation process on the electrode. The capacity of the second cycle was 1463 mA h g^{-1} and the subsequent cycles showed a high reversible capacity has an average C.E. of 99.4%. After 260 cycles, the specific capacities remained 1179 mA h g^{-1}, having the 80.1% retention with respect to the second cycle. The voltage profiles for different cycles at 0.185 A g^{-1} are shown in Fig. 4b. Except for the 1st cycle, those profiles exhibited two potential plateaus observed in the discharge (lithiation) process from 0.9 to 0.6 and 0.4 to 0.1 V. On the other hand, two potential plateaus were observed in the charge (delithiation) process from 0.4 to 0.7 V and 0.9–1.5 V. The profiles trend shifted to the right and then left for the capacity had a promotion in first few cycles, which was owing to the reaction gradually stabilized as the cyclic test. The shape of those

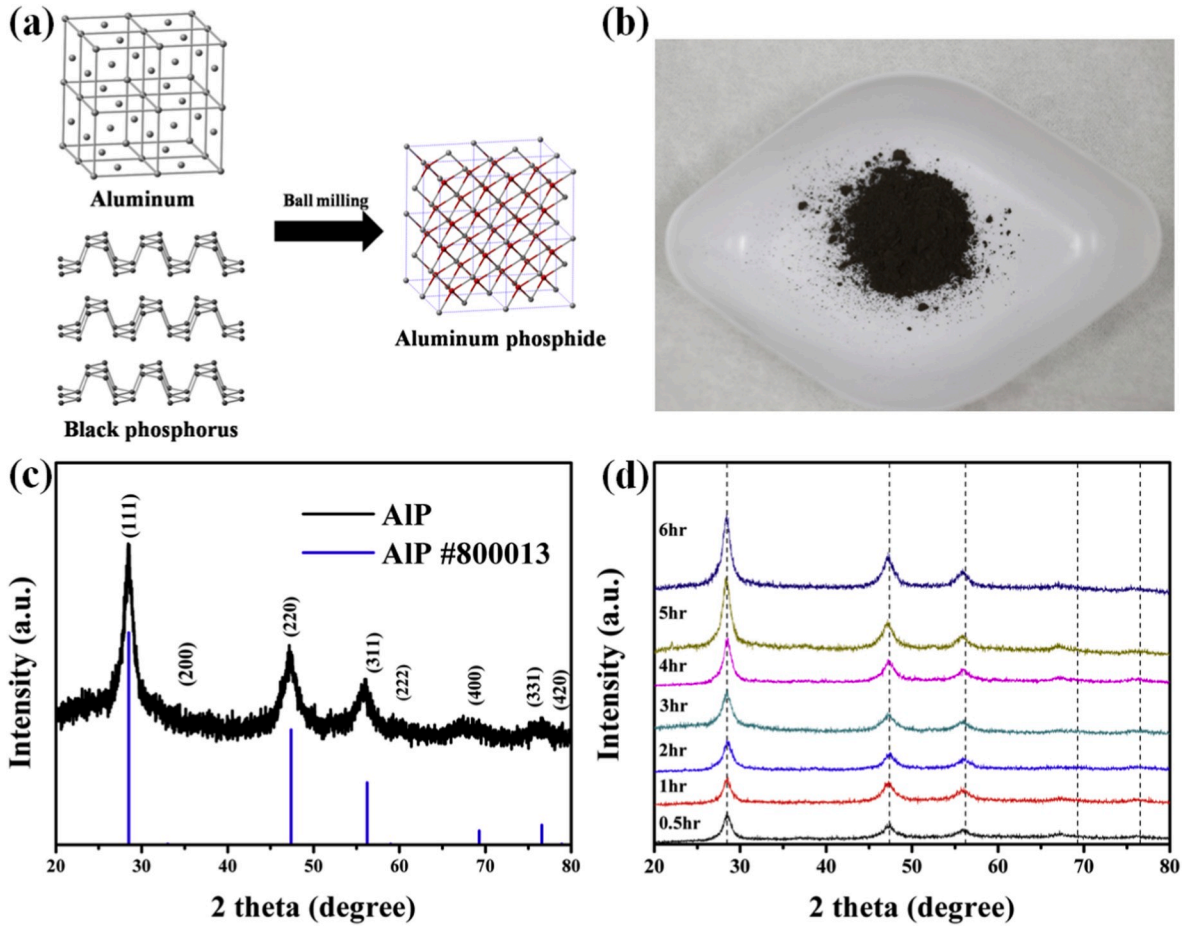

Fig. 1. Synthesis and XRD evolution of AlP. (a) Schematically crystallographic phase change before and after the HEMM. (b) AlP powder. (c) XRD pattern of AlP and JCPDS standard. (d) XRD pattern of AlP with different ball milling times.

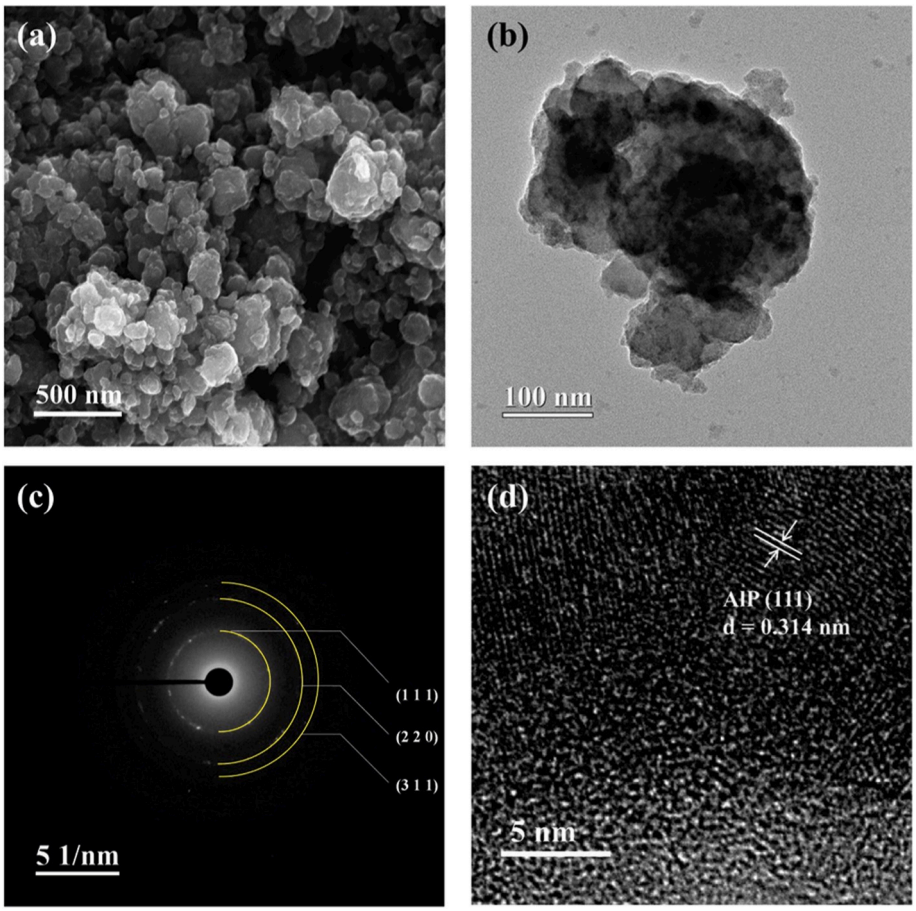

Fig. 2. Morphology of AlP & AlP/CNT mixture and selected area electron diffraction pattern. (a) SEM image of AlP. (b) HRTEM image of AlP. (c) SAED pattern of AlP. (d) HRTEM image of AlP/CNT mixture.

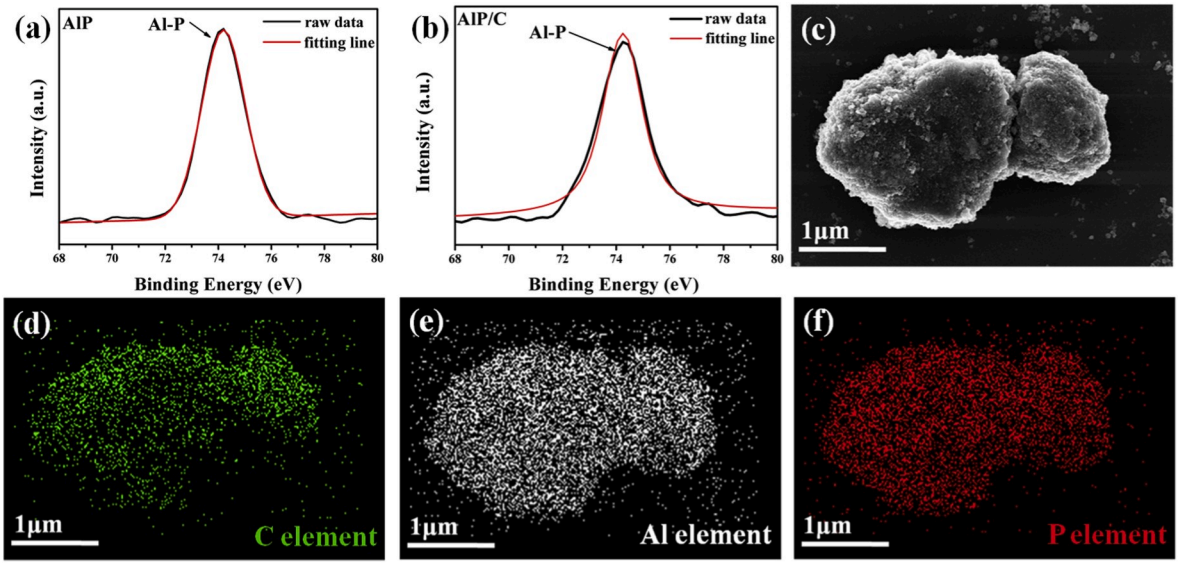

Fig. 3. XPS characteristic of AlP/CNT mixture and EDS mappings. (a) Al-2p spectrum of XPS of AlP. (b) Al-2p spectrum of XPS of AlP/CNT mixture. (c) SEM image of AlP/CNT mixture. (d–f) Element mappings of C, Al, and P by energy-dispersive X-ray spectroscopy.

profiles didn't change drastically, indicating that the performance was stable (there are two small peaks at the 10th cycle profile of the charge because of the power failure). As shown in Fig. 4c, the further study of the lithiation/delithiation process of AlP was made by a cyclic voltammetry (CV) test. The curves were obtained from 0.01 to 3.2 V vs. Li^+/Li at a scanning rate of 0.1 mV S^{-1}. The first cycle had a quite different peak from the other cycles at 0.6 V, attributed to the side reaction and the formation of SEI layer from electrochemical reduction of the electrolyte. Except for the first charge/discharge cycle, there were six mainly peaks. First apparent peak I in the cathodic scan was located at 0.65 V

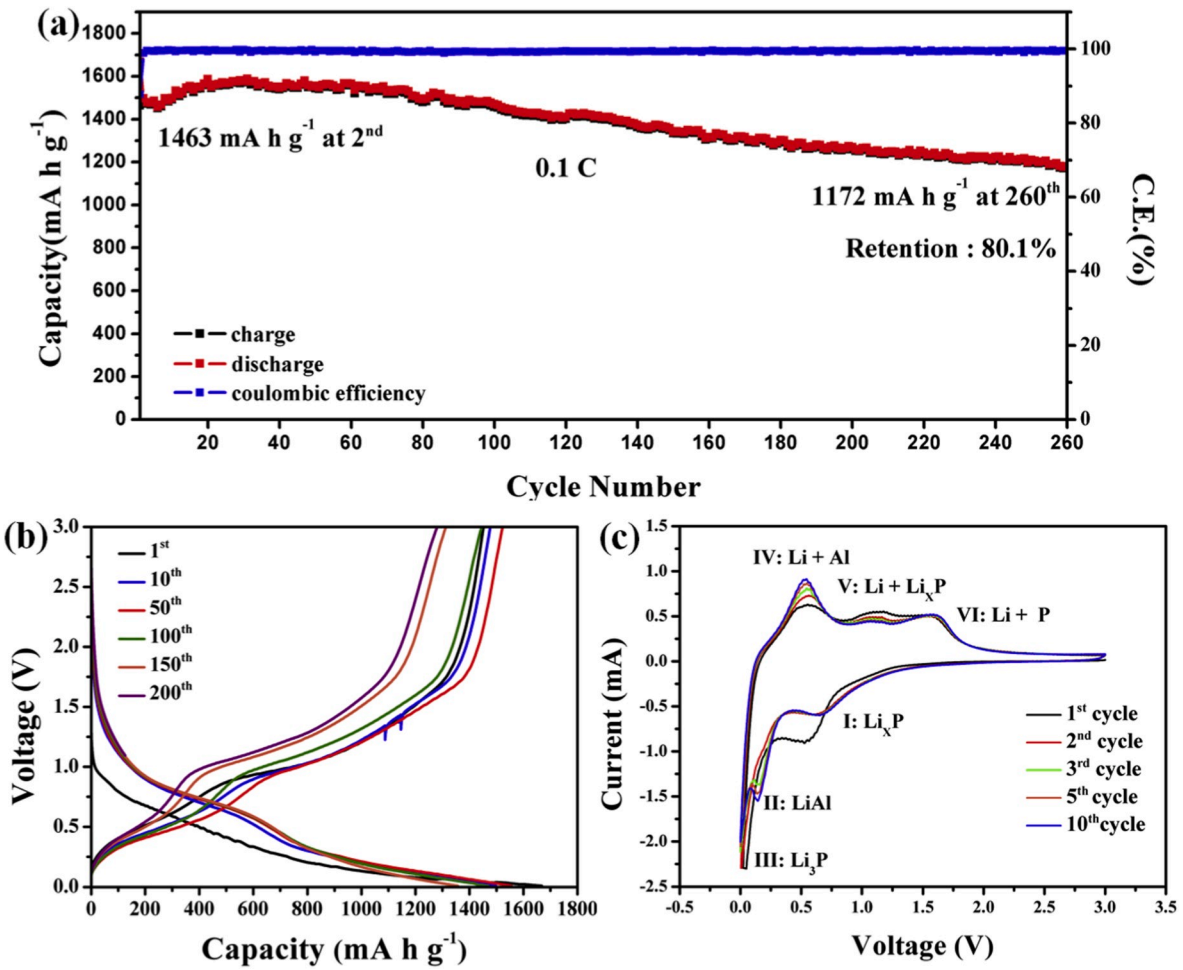

Fig. 4. Electrochemical performance of AlP; 1.85 A g^{-1} = 1C. (a) Galvanostatic cycling test performance of AlP at 0.185 A g^{-1}. (b) Voltage profiles of AlP at 0.185 A g^{-1} between 0.01 and 3.2 V (vs. Li^+/Li). (c) Cyclic voltammetry test of AlP between 0.01 and 3.2 V (vs. Li^+/Li) at scanning rate of 0.1 mV S^{-1}.

which formed the transition metal material, Li_xP (x = 1–3). This reaction was reported by Yu et al. [8,41] The corresponding conversion reaction is AlP + x Li^+ + x e^- → Al + Li_xP. The peak II at 0.15 V formed Li–Al alloy (Al + Li^+ + e^- → LiAl) which was reported by Huang et al. [21] The peak III (0.1–0.01 V) was the final lithiation process to form Li_3P (Li_xP + (3-x) Li^+ + (3-x) e^- → Li_3P), which was reported and confirmed by Park and Shon et al. [10] For the anodic cycle, three peaks IV (0.5 V), V (1.1 V), and VI (1.6 V) were observed. The peak IV revealed that the lithium ions were extracted from LiAl at delithiation. Peak V and VI revealed the lithium ions were extracted from Li_3P phase to Li_xP (x = 1–3) intermediates at delithiation and finally back into P [50]. In conclusion, the lithium alloyed with P at 0.6 and 0.1 V and dealloyed with P at 1.1 and 1.6 V. On the other hand, the lithium alloyed and dealloyed with Al at 0.15 and 0.5 V, respectively. According to this result, the simulated crystal pictures of two steps lithiation mechanism for AlP were represented in Fig. 5. Firstly, the sphalerite-structured ($F\bar{4}3m$) AlP turned into a cubic-structured ($Fm\bar{3}m$) Al and the monoclinic-structured ($P2_1/c$) LiP. Next, Al and LiP alloyed with Li-ion to form a cubic-structured ($Fd\bar{3}m$) LiAl and a hexagonal-structured ($P6_3/mmc$) Li_3P. On the opposite, during the delithiation, LiAl and Li_3P dealloyed to Al and LiP and then recombined into original AlP.

Fig. S5 shows the electrochemistry impedance spectroscopy (EIS) of AlP before and after the cyclic test at frequencies from 10 kHz to 10 mHz with an equivalent circuit. The Nyquist plots composed of two section: a semicircles at the high-frequency region and a straight line slope at low-frequency regions. R_s was the resistance of separate and electrolyte, R_{ct} was the charge transfer resistance between the electrolyte and the

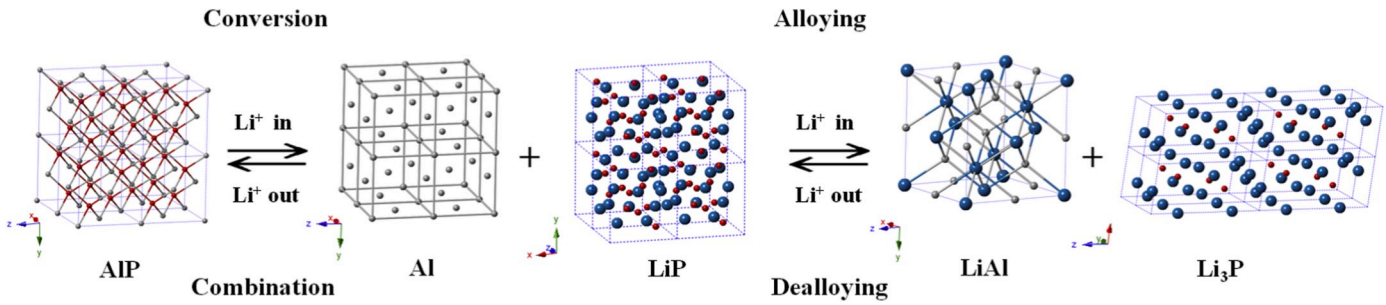

Fig. 5. Simulated illustration of a two-step crystallographic phase change mechanism of AlP during the charge/discharge process.

electrode, C_{dl} was the double layer capacitance on the electrode, and Z_w was the Warburg impedance which described the diffusion of Li^+ in the electrode at solid state [51,52]. The electrode reveal the smaller R_S value and diameter of the semicircle after the cyclic test. Interception with the real impedance axes that AlP had R_s (5.3 Ω) and R_{ct} (62.9 Ω) after the cyclic test and R_s (33.8 Ω) and R_{ct} (102.1 Ω) before the cyclic test. The slope of line at low frequency regions decreased after the cyclic test, which could be attributed to the generation of by-products after the first reaction. All the above results well explained that the performance was promoted after first few cycles. The galvanostatic cycling test was conducted at 1.85 A g^{-1} (1C). As shown in Fig. 6a, the cyclability of AlP achieved 2000 cycles. In the first 3 cycles, the current density of 0.185 A g^{-1} was used to form SEI layer and stabilized the structure. The charge and discharge capacities were 648 and 643 mA h g^{-1} at the 2000th cycle and the retention was 86.5% with respect to the 4th cycle, but the retention is 110.2% with respect to the 20th cycle. This remarkable electrochemical performance of AlP could be attributed to the aluminum for its conductivity and smaller volume change. The SEM images of the pristine anode and the anode after galvanostatic cycling test anode are shown in Fig. S6. After a 2000 cyclic test at 1.85 A g^{-1}, the surface of anode became smooth and flattened compared with the original one. It indicated the material didn't crack after frequent volume changes and maintain the capacity and the conductivity. The rate capability of AlP was evaluated by various charge/discharge rates from 0.5C to 10C. As shown in Fig. 6b, the AlP electrode displays specific charge capacities of 933, 750, 612, 518, 470, 432, and 334 mA h g^{-1} at the rates of 0.925 A g^{-1} (0.5C), 1.85 A g^{-1} (1C), 3.7 A g^{-1} (2C), 5.55 A g^{-1} (3C), 7.4 A g^{-1} (4C), 9.25 A g^{-1} (5C), and 18.5 A g^{-1} (10C), After the 18.5 A g^{-1} test, the rate was immediately returned to 0.925 A g^{-1} and still had the same performance as the initial test at 0.925 A g^{-1}. In the first cycle, the current density of 0.185 A g^{-1} to 92.5 A g^{-1} in Fig. 6c. Under the experimental conditions, the current density of charge at 0.185 A g^{-1} (0.1C), 0.925 A g^{-1} (0.5C), 1.85 A g^{-1} (1C), 5.55 A g^{-1} (3C), 9.25 A g^{-1} (5C), 18.5 A g^{-1} (10C), 37 A g^{-1} (20C), 55.5 A g^{-1} (30C), 74 A g^{-1} (40C), and 92.5 A g^{-1} (50C) with the fixed discharge current density at 0.185 A g^{-1} (0.1C). AlP showed performance with the specific charge capacities of 1458, 1379, 1407, 1302, 1240, 1120, 930, 727, 525, and 452 mA h g^{-1} at corresponding current density, respectively. After the 92.5 A g^{-1} test, the charge rate was immediately returned to 1.85 Ω A g^{-1} and the specific capacity still had over 1400 mA h g^{-1}. Those results pointed that lithiation and delithiation process still occurred at high rates [53].

In this study, MWCNT was used to replace super-P as a conductive agent. As shown in Fig. S7a, MWCNT could provide better performance and stability of battery than super-P. Also, as shown in Fig. S7b, it indicates that MWCNT had smaller charge transfer resistance between the electrolyte and electrode than super-P. The EIS test was at frequencies from 10 kHz to 10 mHz. The R_{ct} of AlP/CNT mixture was 102.1 Ω and the R_{ct} of AlP/super-P mixture was 163.9 Ω. As shown in Fig. S8, although the structure of MWCNT was disrupted after 24 h ball milling, the electrical properties of MWCNT still existed and MWCNT closely attached to the surface of AlP to consolidate the structure of AlP [54,55]. Additionally, three electrolytes were tested to find the optimized capability for AlP in LIB. As shown in Fig. S9b, the FEC-based electrolyte provided well assistance for AlP in LIB, it could be attributed to FEC can form a thinner and more stable SEI layer than the EC-derived SEI [56]. Also, FEC/DEC (1:1 vol%) electrolyte exhibited more capacity than FEC/DEC (3:7 vol%) electrolyte. The growth of the solid electrolyte interface (SEI) on the surface of the active material is a well-known phenomenon that occurs during cycling. It has been found that for high-capacity materials, the use of FEC as an additive can result in high-performance electrode. However, the brittle SEI may be broken due

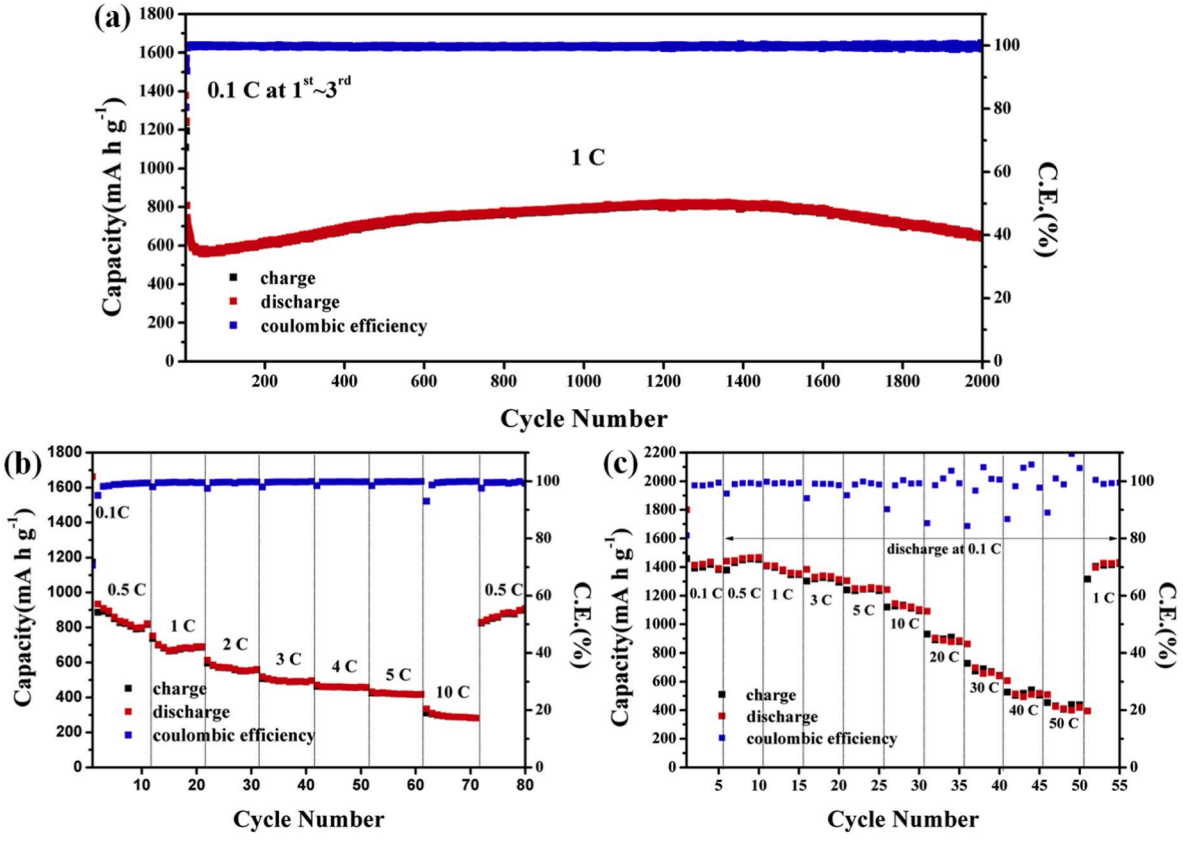

Fig. 6. Electrochemical performance of AlP at long-term and high rate capability test. (a) Galvanostatic cycling test performance of AlP at 1.85 A g^{-1}. (b) Galvanostatic cycling rate capability test performance of AlP at various current density from 0.925 to 18.5 A g^{-1}. (c) Galvanostatic cycling rate capability test performance of AlP at various current density of charge from 0.185 A g^{-1} to 92.5 A g^{-1} with fixed discharge current density at 0.185 A g^{-1}.

to expansion and contraction of the active materials during the cycle, and then the active surface is exposed to the electrolyte again, leading to the reformation of SEI and makes the SEI thicker for each cycle. The electrolyte system with FEC can stabilize the SEI membrane and reduce the impedance for the lithiation/delithiation process. Compared with the electrolyte system with EC:DMC as shown in Fig. S9, the electrolyte added with FEC can make the SEI layer thinner and more compact, and also provide a shorter path for the diffusion of lithium ions in the AlP/C electrode, so as to improve the cycle performance.

The full cell comprising AlP anode and commercial $LiFePO_4$ cathode were assembled to demonstrate the viability of AlP as a LIB anode. Firstly, the cutoff voltage was required for a full cell to accord the potential plateaus. Next, the simulated curve could be obtained by subtracting the discharge curve of AlP from the charge curve of $LiFePO_4$ and subtracting the charge curve of AlP from the discharge curve of $LiFePO_4$ in their respective half-cells. Fig. 7a and b shows the simulation of charge/discharge curve of the AlP–$LiFePO_4$ full cell. The real full cell curve behaved similarly to the simulated curve, which evidenced that the actual full cell had no side reaction during the operation. The voltage plateau located about 2.5 and 3.2 V at charge process and about 2.9 and 2.4 V at discharge process.

The galvanostatic cycling test of the coin-type full cell at a current density of 0.185 A g^{-1} is shown in Fig. 7c. The capacities were 0.99 mA h at the 85th cycle which had 79.8% retention with respect to the 2nd cycle. The specific capacities were also around 1100 mA h g^{-1}. The voltage profiles of the AlP–$LiFePO_4$ full cell at different cycles was shown in Fig. 7d. Furthermore, a 3 cm × 6 cm pouch-type battery was assembled. Fig. 8a shows the galvanostatic cycling test performance of the pouch-type battery. The capacities were nearly 14 mA h and the cycle life (over 80% retention) was more than 80 cycles which could light up hundreds of LED bulbs to display the word "AlP anode LIBs" with three different colors (Fig. 8b). Fig. 8c shows the battery to power the fan. The corresponding video was shown in supporting information.

4. Conclusions

AlP is prepared and used as LIB anodes for the first time. AlP anode exhibits high reversible capacities of 1463 mA h g^{-1} at 0.185 A g^{-1}, high rate capability at 92.5 A g^{-1}, and excellently long-term cycle life of 2000 cycles at 1.85 A g^{-1}. A cyclic voltammetry (CV) test of AlP confirms the lithiation process of AlP a conversion reaction. Initially, AlP reacting with Li turned into Al and LiP, and then, Al and LiP alloyed with Li ion to form LiAl and Li_3P. The coin-type and the pouch-type full battery using AlP as the anode and $LiFePO_4$ as the cathode are assembled as a proof of concept demonstration to turn on electronic devices. This study highlights AlP a high performance anode material with earth abundance for use on LIBs.

Declaration of competing interest

The authors declare that they have no known competing financial interests or personal relationships that could have appeared to influence the work reported in this paper.

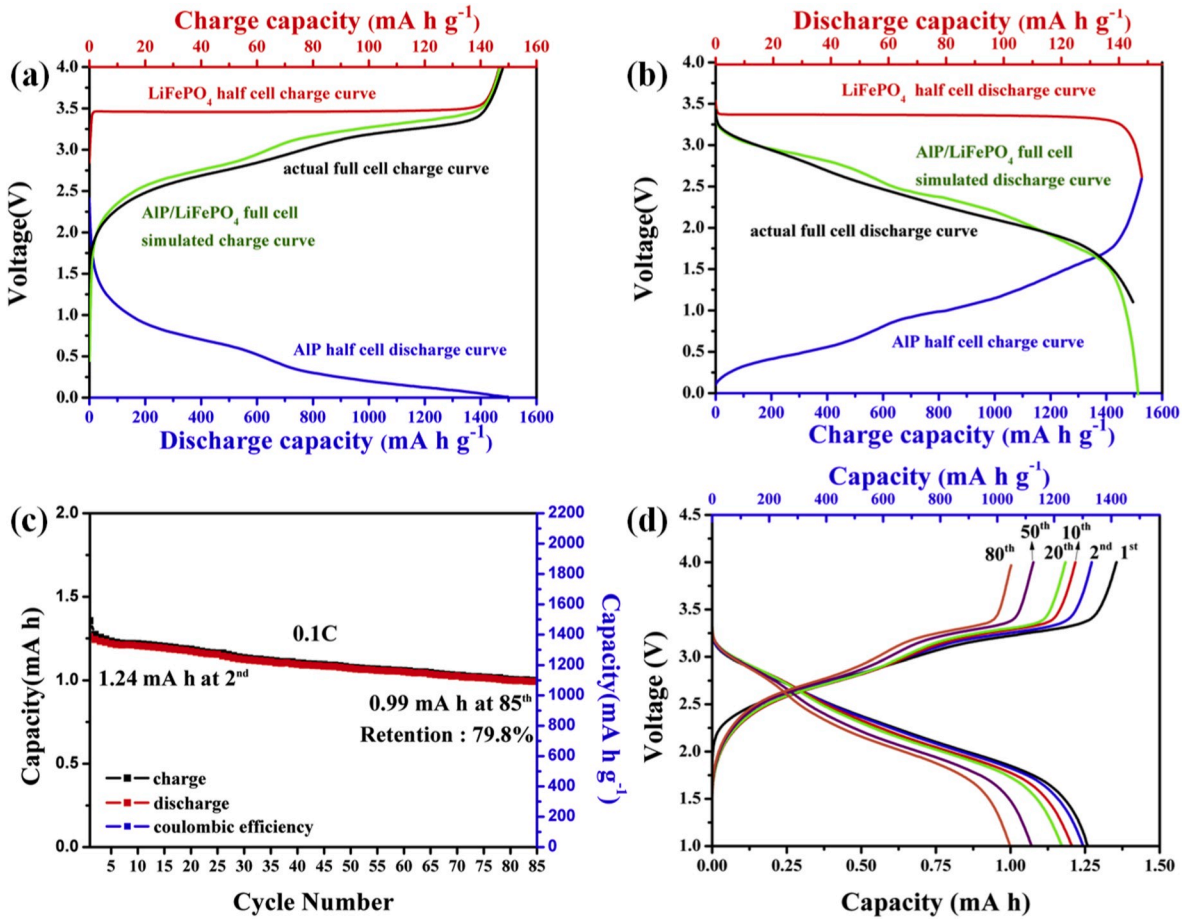

Fig. 7. Simulated curves of voltage profiles of AlP–$LiFePO_4$ full cell at 0.185 A g^{-1} and electrochemical performance of AlP–$LiFePO_4$ full cell. (a) Simulated curve of charge of the full cell by using AlP half cell discharge curve and $LiFePO_4$ half cell charge curve. (b) Simulated curve of discharge of the full cell by using AlP half cell charge curve and $LiFePO_4$ half cell discharge curve. (c) Galvanostatic cycling test performance of AlP–$LiFePO_4$ full cell at 0.185 A g^{-1}. (d) Voltage profiles of AlP–$LiFePO_4$ full cell between 1 and 4 V (vs. Li^+/Li) at 0.185 A g^{-1}.

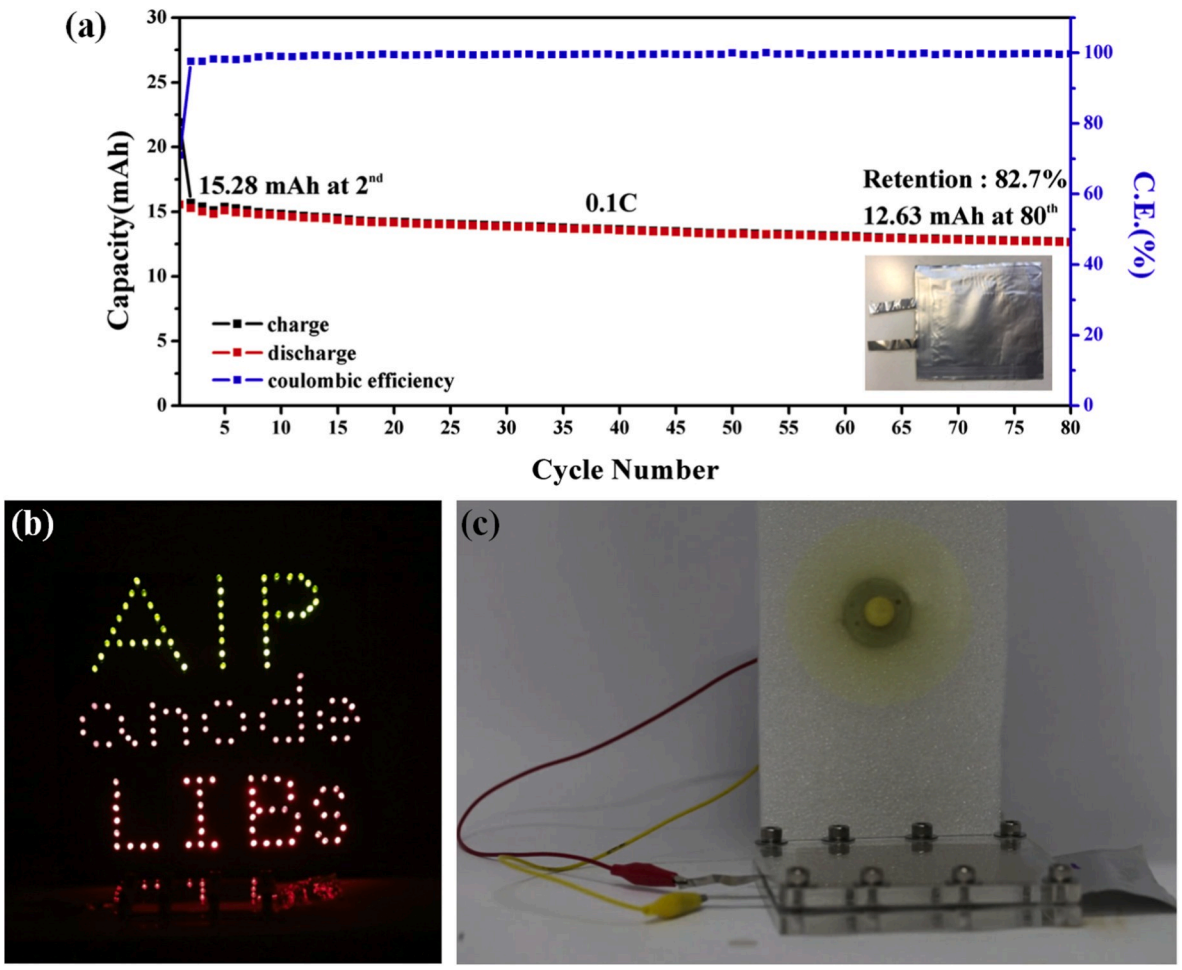

Fig. 8. Demonstration of electrical appliances. (a) Galvanostatic cycling test performance of AlP–$LiFePO_4$ pouch-type full cell at 0.185 A g^{-1}. (b) The demonstration of pouch-type battery lighted up three different color LED bulbs. (c) The demonstration of pouch-type battery drove the fan. (For interpretation of the references to color in this figure legend, the reader is referred to the Web version of this article.)

CRediT authorship contribution statement

Hsuan-Peng Lin: Investigation, Visualization. **Kuan-Ting Chen:** Methodology. **Che-Bin Chang:** Data curation. **Hsing-Yu Tuan:** Conceptualization, Methodology, Writing - review & editing, Supervision.

Acknowledgement

This work was financially supported from the Young Scholar Fellowship Program by Ministry of Science and Technology in Taiwan, under Grant of MOST 108-2636-E-007-013 and MOST 106-2622-8-007-017. The authors also acknowledge the financial support of National Tsing Hua University through the grant of 107Q2708E1.

Appendix A. Supplementary data

Supplementary data to this article can be found online at https://doi.org/10.1016/j.jpowsour.2020.228262.

References

[1] J.M. Tarascon, M. Armand, Nature 414 (2001) 359–367.
[2] V. Etacheri, R. Marom, R. Elazari, G. Salitra, D. Aurbach, Energy Environ. Sci. 4 (2011) 3243–3262.
[3] C.L. Xu, W. Xiang, Z.G. Wu, Y.D. Xu, Y.C. Li, M.Z. Chen, G.X. Dong, G.P. Lv, J. Zhang, B.H. Zhong, *ACS Appl. Mater. Interfaces* 10 (2018) 27821–27830.
[4] Y.D. Xu, W. Xiang, Z.G. Wu, C.L. Xu, Y.C. Li, X.D. Guo, G.P. Lv, X. Peng, B. H. Zhong, Electrochim. Acta 268 (2018) 358–365.
[5] L. Zeng, Y. Fang, L. Xu, C. Zheng, M.Q. Yang, J. He, H. Xue, Q. Qian, M. Wei, Q. Chen, Nanoscale 11 (2019) 6766–6775.
[6] C. Xu, W. Xiang, Z. Wu, Y. Xu, Y. Li, Y. Wang, Y. Xiao, X. Guo, B. Zhong, ACS Appl. Mater. Interfaces 11 (2019) 16629–16638.
[7] W. Yang, N. Luo, C. Zheng, S. Huang, M. Wei, Small 15 (2019) 1903904.
[8] W.C. Chang, K.W. Tseng, H.Y. Tuan, Nano Lett. 17 (2017) 1240–1247.
[9] S. Carenco, D. Portehault, C. Boissiere, N. Mezailles, C. Sanchez, Chem. Rev. 113 (2013) 7981–8065.
[10] E.P. Pandres, J.Z. Olson, C.W. Schlenker, V.C. Holmberg, ACS Appl. Energy Mater. 2 (2019) 6200–6208.
[11] S. Foley, H. Geaney, G. Bree, K. Stokes, S. Connolly, M.J. Zaworotko, K.M. Ryan, Adv. Funct. Mater. 28 (2018) 1800587.
[12] C.M. Park, H.J. Sohn, Adv. Mater. 19 (2007) 2465–2468.
[13] L. Wang, X.M. He, J.J. Li, W.T. Sun, J. Gao, J.W. Guo, C.Y. Jiang, Angew. Chem. Int. Ed. 51 (2012) 9034–9037.
[14] G.C. Guo, X.L. Wei, D. Wang, Y.P. Luo, L.M. Liu, J. Mater. Chem. 3 (2015) 11246–11252.
[15] S. Carenco, D. Portehault, C. Boissiere, N. Mezailles, C. Sanchez, Adv. Mater. 26 (2014) 371–390.
[16] J.F. Qian, D. Qiao, X.P. Ai, Y.L. Cao, H.X. Yang, Chem. Commun. 48 (2012) 8931–8933.
[17] T. Ramireddy, T. Xing, M.M. Rahman, Y. Chen, Q. Dutercq, D. Gunzelmann, A. M. Glushenkov, J. Mater. Chem. 3 (2015) 5572–5584.
[18] G. Wang, F. Li, D. Liu, D. Zheng, C.J. Abeggien, Y. Luo, X. Yang, T. Ding, D. Qu, Energy Storage Mater. 24 (2020) 147–152.
[19] K. Wu, G. Xu, D. Pan, M. Wu, Chem. Eng. J. 385 (2020) 123456.
[20] Y. Li, S. Jiang, Y. Qian, Y. Han, J. Zhou, T. Li, L. Xi, N. Lin, Y. Qian, Chem. Commun. 55 (2019) 6751–6754.
[21] J.B. Zhou, Z.H. Jiang, S.W. Niu, S.S. Zhu, J. Zhou, Y.C. Zhu, J.W. Liang, D.D. Han, K.L. Xu, L.Q. Zhu, X.J. Liu, G.M. Wang, Y.T. Qian, Inside Chem. 4 (2018) 372–385.
[22] W. Liu, H. Zhi, X. Yu, Energy Storage Mater. 16 (2019) 290–322.
[23] M. Ihsan-Ul-Haq, H. Huang, J. Cui, S. Yao, J. Wu, W.G. Chong, B. Huang, J.K. Kim, J. Mater. Chem. 6 (2018) 20184–20194.

[24] W. Li, X. Li, J. Liao, B. Zhao, L. Zhang, L. Huang, G. Liu, Z. Guo, M. Liu, Energy Environ. Sci. 12 (2019) 2286–2297.
[25] R. Muruganantham, P. Chiang, W. Liu, ACS Appl. Energy Mater. 1 (2018) 3674–3683.
[26] S. Shi, Z. Li, Y. Sun, B. Wang, Q. Liu, Y. Hou, S. Huang, J. Huang, Y. Zhao, Nano Energy 48 (2018) 510–517.
[27] T.T. Nguyen, J. Balamurugan, N.H. Kim, J.H. Lee, J. Mater. Chem. 6 (2018) 8669–8681.
[28] W. Li, Q. Yang, S. Chou, J. Wang, H. Liu, J. Power Sources 294 (2015) 627–632.
[29] W. Li, J. Yu, J. Wen, J. Liao, Z. Ye, B. Zhao, X. Li, H. Zhang, M. Liu, Z. Guo, J. Mater. Chem. 7 (2019) 16785–16792.
[30] W. Li, X. Li, J. Yu, J. Liao, B. Zhao, L. Huang, A. Abdelhafiz, H. Zhang, J.H. Wang, Z. Guo, M. Liu, Nano Energy 61 (2019) 594–603.
[31] W. Zhang, W.K. Pang, V. Sencadas, Z. Guo, Joule 2 (2018) 1534–1547.
[32] X. Wang, H.M. Kim, Y. Xiao, Y.K. Sun, J. Mater. Chem. 4 (2016) 14915–14931.
[33] S. Boyanov, F. Gillot, L. Monconduit, Ionics 14 (2008) 125–130.
[34] J. Zhu, Q. He, Y. Liu, J. Key, S. Nie, M. Wu, P.K. Shen, J. Mater. Chem. 7 (2019) 16999–17007.
[35] Y. Wang, Q. Fu, C. Li, H. Li, Hua Tang, ACS Sustain. Chem. Eng. 6 (2018) 15083–15091.
[36] S. Li, J.J. Niu, Y.C. Zhao, K.P. So, C. Wang, C.A. Wang, J. Li, Nat. Commun. 6 (2015).
[37] M. Au, S. McWhorter, H. Ajo, T. Adams, Y.P. Zhao, J. Gibbs, J. Power Sources 195 (2010) 3333–3337.
[38] S.K. Sharma, M.S. Kim, D.Y. Kim, J.S. Yu, Electrochim. Acta 87 (2013) 872–879.
[39] Y.G. Huang, X.L. Lin, Q.C. Pan, Q.Y. Li, X.H. Zhang, Z.X. Yan, X.M. Wu, Z.Q. He, H. Q. Wang, Electrochim. Acta 193 (2016) 253–260.
[40] J.H. Park, C. Hudaya, A.Y. Kim, D.K. Rhee, S.J. Yeo, W. Choi, P.J. Yoo, J.K. Lee, Chem. Commun. 50 (2014) 2837–2840.
[41] Q.F. Li, N.J. Bjerrum, J. Power Sources 110 (2002) 1–10.
[42] Y. Hamon, T. Brousse, F. Jousse, P. Topart, P. Buvat, D.M. Schleich, J. Power Sources 97–8 (2001) 185–187.
[43] C.R. Ryder, J.D. Wood, S.A. Wells, Y. Yang, D. Jariwala, T.J. Marks, G.C. Schatz, M. C. Hersam, Nat. Chem. 8 (2016) 598–603.
[44] F. Niu, L.M. Tao, Y.C. Deng, Q.H. Wang, W.G. Song, New J. Chem. 38 (2014) 2269–2272.
[45] J. Sun, G.Y. Zheng, H.W. Lee, N. Liu, H.T. Wang, H.B. Yao, W.S. Yang, Y. Cui, Nano Lett. 14 (2014) 4573–4580.
[46] C. Hinnen, D. Imbert, J.M. Siffre, P. Marcus, Appl. Surf. Sci. 78 (1994) 219–231.
[47] N.M. Figueiredo, N.J.M. Carvalho, A. Cavaleiro, Appl. Surf. Sci. 257 (2011) 5793–5798.
[48] C.P. Pan, W.X. Li, S.R. Jiang, Int. J. Mol. Sci. 6 (2005) 198–202.
[49] L. Qiu, W. Xiang, W. Tian, C.L. Xu, Y.C. Li, Z.G. Wu, T.R. Chen, K. Jia, D. Wang, F. R. He, X.D. Guo, Nano Energy 63 (2019) 103818.
[50] Z.X. Yu, J.X. Song, M.L. Gordin, R. Yi, D.H. Tang, D.H. Wang, Adv. Sci. 2 (2015).
[51] M.W. Forney, M.J. Ganter, J.W. Staub, R.D. Ridgley, B.J. Landi, Nano Lett. 13 (2013) 4158–4163.
[52] X. Li, J.P. Rong, B.Q. Wei, ACS Nano 4 (2010) 6039–6049.
[53] A.S. Arico, P. Bruce, B. Scrosati, J.M. Tarascon, W. Van Schalkwijk, Nat. Mater. 4 (2005) 366–377.
[54] N. Pierard, A. Fonseca, J.F. Colomer, C. Bossuot, J.M. Benoit, G. Van Tendeloo, J. P. Pirard, J.B. Nagy, Carbon 42 (2004) 1691–1697.
[55] J.X. Song, Z.X. Yu, M.L. Gordin, X.L. Li, H.S. Peng, D.H. Wang, ACS Nano 9 (2015) 11933–11941.
[56] Y.M. Lin, K.C. Klavetter, P.R. Abel, N.C. Davy, J.L. Snider, A. Heller, C.B. Mullins, Chem. Commun. 48 (2012) 7268–7270.